JOURNAL OF CATALYSIS **161,** 401–408 (1996)
ARTICLE NO. 0198

In Situ Generation of Palladium Nanoparticles in Smectite Clays

Zoltán Király,*[,1] Imre Dékány,* Ágnes Mastalir,† and Mihály Bartók†

*Department of Colloid Chemistry, Attila József University, Aradi Vt. 1, and †Department of Organic Chemistry, Attila József University, Dóm tér 8, H-6720 Szeged, Hungary

Received July 6, 1995; revised February 12, 1996; accepted February 14, 1996

A novel synthetic route has been developed for the preparation of clay intercalated palladium catalysts. Liquid sorption and X-ray diffraction measurements on ethanol(1)–toluene(2)/hexadecylammonium montmorillonite dispersions indicated that a toluene-rich bulk liquid phase was equilibrated with a swollen, ethanol-rich interlamellar phase having a volume of about 0.9 cm^3/g organoclay. Introduction of palladium(II) acetate into the organoclay suspension led to the generation and deposition of a metallic palladium dispersion in the interlamellar space. This system behaved as a versatile nanophase reactor, wherein the ethanol functioned as both solvent and reducing agent. The progress of the $Pd^{2+} \rightarrow Pd^0$ reaction was monitored spectrophotometrically. The ethanolic reduction afforded Pd particles 2 to 14 nm in diameter, depending on the experimental conditions, deposited on clay particle defect sites. Organoclays loaded up to 10 mass% Pd were synthesized and characterized by BET surface area analysis, transmission electron microscopy, low-shear rheology, X-ray diffraction, and small-angle X-ray scattering measurements. The Pd–organoclay samples proved to be catalytically active in olefin hydrogenation in the liquid phase.

INTRODUCTION

Recent advances in organic synthesis in which smectite clays were used as catalysts or catalyst supports have led to a rational approach to the design of new heterogeneous catalysts (1). There are two major classes: pillared clays and metal complex-layered silicate intercalation catalysts (2).

Polyoxycation-exchange forms of smectites can be transformed, on heating, into pillared clays. These thermally stable microporous materials contain large metal oxide clusters in the interlamellar space, with gallery heights of about 1 nm (1–8). Direct intercalations of metal oxide sol particles in the interlamellar space of swelling clays have also been reported to produce well-defined pillared layered silicates (9). The catalytic activity of pillared clays is mostly attributed to the acidic gallery sheets rather than to the props (1–3), but the intracrystal pillaring agent itself may also be regarded as the catalytic species (4–7). The molecular pathway to the attainment of metal dispersions on pillared clays offers more specificity than achieved with conventional impregnation methods (10). Among the advantages of pillared smectite clays over faujasitic zeolites is that their pore size can be made larger and, under controlled pillaring conditions, the pore size can be adjusted to suit a particular application [clay catalyst engineering (8)].

The second class, metal complex-layered silicate intercalation catalysts, may be regarded as heterogenized homogeneous catalysts. Pd, Rh, and Ru chelates have been immobilized by intercalation in swelling layered silicates and applied mostly in hydrogenation reactions (11–15). The advantage of anchored catalysts over the corresponding homogeneous derivatives is the heterogenized homogeneous catalysts can readily be reclaimed from the reaction mixture. On the other hand, the interlayer distance can be adjusted to the desired value by a careful selection of the reaction medium which will ensure increased stereoselectivity. Surface chemical effects on catalytic selectivity can be equally important.

In this paper a novel synthetic route leading to a new class of smectite clay catalysts is proposed. The idea is based on a combination of two independent observations. First, palladium subcolloids (2–6 nm in diameter) have been synthesized from palladium(II) complexes in the presence of polyvinylpyrrolidone as a steric stabilizer (16, 17). Various alcohols may act both as solvent and as reducing agent (17). Second, CdS and ZnS semiconductor nanoparticles (10–20 nm) have been generated *in situ* in the adsorption layer of hexadecylpyridinium (HDP) montmorillonite suspended in binary solvent systems (18). The selective sorption of methanol or ethanol from cyclohexane solution provided a suitable environment in the clay host (referred to as a nanophase reactor) for the reaction of Cd^{2+} and Zn^{2+} acetates with H_2S to produce intercalated metal sulfide nanocrystallites. On the basis of these observations, it seemed reasonable to attempt to generate palladium nanoparticles *in situ* in the interlamellar space of surfactant-modified smectites (clay organocomplexes) in alcohol–hydrocarbon binary liquid mixtures. The strategy of the controlled colloid synthesis may be given as follows:

[1] To whom correspondence should be addressed. Fax: 36-62-312921.

0021-9517/96 $18.00

1. Selection of the alcohol–hydrocarbon liquid pair: The hydrocarbon must be a reasonably good solvent for the palladium compound, and the alcohol must be a reducing agent for the palladium cation.

2. Selection of the clay organocomplex: The preferential adsorption of the alcohol over the hydrocarbon component should produce an alcohol-rich interlayer composition, accompanied by uniaxial swelling of the basal planes to ensure sufficient space for particle generation.

3. Immobilization of the palladium subcolloids in the clay host.

4. Elimination or at least minimization of the reduction of palladium ions leading to particle formation in the bulk solution: A hydrocarbon-rich bulk solution is desired.

5. Monitoring of the progress of formation of intercalated palladium particles.

Several systems might comply with the aforementioned expectations. In this work, ethanol(1)–toluene(2)/hexadecylammonium montmorillonite (HDAM) and palladium (II) acetate [$Pd(OAc)_2$] have been selected for use.

EXPERIMENTAL

Materials. HDAM was prepared by cation-exchange reaction between fractionated Na^+ montmorillonite [Südchemie AG, Germany, particle size $d < 2$ μm, cation-exchange capacity (CEC) = 82 mEq/100 g] and hexadecylammonium bromide (Fluka AG, Switzerland) (19–21). The organocomplex was purified by Soxhlet extraction in a 2-propanol : water = 1 : 1 mixture for 50 h, freeze-dried from benzene, and dried in a vacuum desiccator at 343 K overnight before use. Palladium(II) acetate, $Pd(OAc)_2$, was purchased from ABCR GmbH, Germany (quoted purity 99%), and used as received. Ethanol and toluene (Reanal, Hungary) were distilled and stored over a 0.4-nm molecular sieve (Merck AG, Germany).

Synthesis. A typical preparation is described. HDAM (1.0 g) was suspended in 100 cm^3 of an ethanol : toluene = 5 : 95 mixture in a 250-cm^3 three-necked round-bottom flask. After adsorption equilibration had been attained, 30 cm^3 of 1% $Pd(OAc)_2$ in toluene solution was introduced into the system. The suspension was stirred magnetically and the reaction was left to proceed at room temperature. The yellow suspension became progressively darker as reduction proceeded, and turned black within 1 h. The progress of the reduction of Pd^{2+} to Pd^0 was monitored spectrophotometrically. Samples of 1 cm^3 were periodically removed from the reaction flask and centrifuged for 10 min at 4000 *g*, and the pure, yellowish supernatant solutions of $Pd(OAc)_2$ were analyzed at $\lambda = 397$ nm with a Uvikon 930 spectrophotometer. The absorbance by $Pd(OAc)_2$ varied linearly in the concentration range of interest. Thus, a separate calibration curve permitted a quantitative conversion of the $Pd(OAc)_2$ consumption into the formation of Pd^0 particles. Variation in the reaction time and in the composition of the system afforded a metallic Pd content as high as 10 mass%. Blank runs with no organoclay or with no ethanol in the reaction mixture, but under otherwise the same experimental conditions, were also performed to confirm that Pd^{2+} consumption was due to Pd^0 formation in the adsorption layer but not in the bulk solution. After the desired Pd^0 content had been achieved, the Pd^0–organoclay was purified in toluene by several centrifugation–redispersion cycles and finally freeze-dried from benzene. The solid samples varied from light gray to black in color, depending on their palladium content. Alcohols and clays different from those reported in this work have also been applied successfully, e.g., 1-propanol, 1-pentanol, octadecylammonium vermiculite, and alumina-pillared montmorillonite.

Adsorption measurements. The adsorption excess isotherm of the ethanol(1)–toluene(2)/HDAM system was determined at 298 K by the immersion method (22, 23), with the use of a Zeiss interferometer and a Paar DMA 58 density meter for the concentration analysis. n^0 mol of liquid (10 cm^3) having an ethanol mole fraction of x_1^0 was equilibrated with $m = 0.4$ g of solid, and the supernatant composition x_1 was analyzed. The most frequently used measure of the adsorption at the solid/liquid interface is the molar reduced adsorption excess amount (22). It was calculated for ethanol via the relation $n_1^{\sigma(n)} = n^0(x_1^0 - x_1)/m$ and the adsorption excess isotherm was constructed as $n_1^{\sigma(n)}$ versus x_1 (22, 23).

BET surface area analysis. The specific surface areas of HDAM and Pd^0–HDAM samples were determined by the BET nitrogen method with a Gemini 2375 automated gas sorption apparatus. The freeze-dried samples in the sorption vessel were pretreated at 343 K under vacuum ($p < 10^{-3}$ Torr) for 2 h.

Transmission electron microscopy. Particle sizes were determined from electron micrographs taken on an OPTON 902 transmission electron microscope at 80 kV. One drop of dilute colloidal dispersion in ethanol was placed on a Formvar grid and allowed to stand for 30–40 s. After solvent evaporation, electron micrographs were taken of the particles retained on the film. Particle sizes were determined by measuring 80–120 particles on magnified transmission electron microscope images.

X-ray diffraction. Variation of the basal spacing of the organoclay with solvent composition was monitored with a Philips X-ray diffractometer (generator: PW 1830, goniometer: PW 1820, detector: PW 1711), Cu $K\alpha$ radiation ($\lambda = 0.154$ nm) being used at 40 kV and 35 mA. To prevent solvent evaporation, the sample holder was covered with a Mylar film. The investigated scattering angle

range of $1^\circ \le 2\theta \le 10^\circ$ for the suspensions was extended to $30^\circ \le 2\theta \le 50^\circ$ for the dry clay samples. The basal plane distances d_L were calculated from the first-order (001) Bragg reflections by using the PW 1877 automated powder diffraction software.

Small-angle X-ray scattering. Measurements were made by using a compact Kratky Camera (Anton Paar, Model KCEC 1129) with an 80 μm × 1.5 cm entrance slit and a 100 μm × 1.5 cm detector slit. Samples were pelleted into the 0.5 × 2 × 15-mm slit of a copper sample holder and measurements were performed for 3 h under a He atmosphere. The scattered X-ray intensities I_s as a function of a scattering angle θ [or the scattering wavevector $h = (4\pi/\lambda)\sin\theta$] were determined by using a PW 1710 control unit and Philips small-angle X-ray scattering (SAXS) control software. The normalized scattering intensity I was calculated from $I = I_s N_0/N_s$, where N_s and N_0 are the intensity counts of the sample and background (in the absence of the sample holder in the cell) in the line-shaped primary beam determined by the moving slit method, and I_s is the measured (smeared) scattering intensity of the sample (18). Blank correction was made to obtain corrected intensities defined by $\Delta I = I(\mathrm{Pd^0}\text{–HDAM}) - I(\mathrm{HDAM})$.

Low-shear rheology. Steady-flow measurements of HDAM and Pd^0–HDAM suspensions (2% in toluene) were performed by using a Couette-type rotation viscosimeter (HAAKE Rotovisco RV-20, CV-100) and an ME-30 sensor system at 25°C. Shear stress (τ) versus shear rate gradient (D) was monitored continuously for 2 min in the range 0 to 100 s^{-1}, controlled by a PG-242 programmer. The suspensions were presheared at the highest shear rate for 2 min.

RESULTS AND DISCUSSION

Adsorption and XRD Measurements on HDAM Suspensions

The adsorption excess isotherm of ethanol(1)–toluene (2)/HDAM is shown in Fig. 1. The experimental data were fitted with an empirical equation (solid line), which was used in subsequent calculations. The isotherm is of type III in the Schay–Nagy classification (23). The adsorption of ethanol from toluene is strongly preferential. Variation of the basal spacing d_L with the ethanol mole fraction x_1 is also plotted in Fig. 1. The relationship is remarkably linear and the fitted straight line was used in subsequent calculations. A quantitative description of the adsorption layer as a nanophase reactor may be given as follows. The molar reduced surface excess amount $n_1^{\sigma(n)}$ is related to the real amount $n^s = n_1^s + n_2^s$ actually present in the adsorption layer via the Ostwald–de Izaguirre equation (23)

$$n_1^{\sigma(n)} = n_1^s x_2 - n_2^s x_1 = \frac{V_1^s \Phi_2 - V_2^s \Phi_1}{V_{m,1}\Phi_2 + V_{m,2}\Phi_1}, \qquad [1]$$

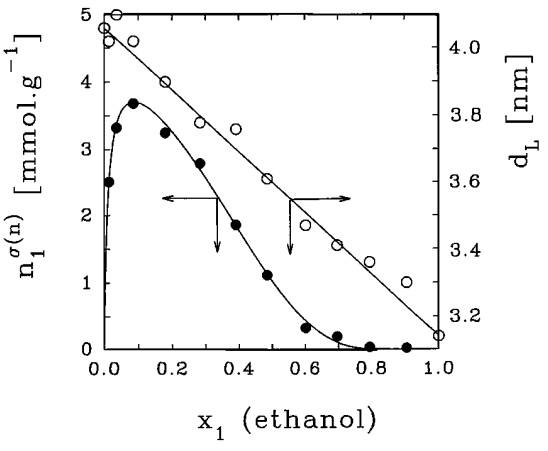

FIG. 1. Adsorption excess isotherm (●) and basal spacings (○) in ethanol(1)–toluene(2)/HDAM suspension at 298 K.

where V_i^s is the volume of the ith component ($i = 1, 2$) in the adsorption layer, $V_{m,i}$ is the (partial) molar volume, and Φ_i is the volume fraction of the ith component in the bulk liquid phase. On the other hand, the free interlamellar space V^s (volume of the nanophase reactor) filled with the two adsorbed components [pore-filling model (22)], can be taken as the difference between the interlamellar volume V_{int} of the (swollen) organoclay and the volume V_{alk} occupied by the alkyl chains anchored to the gallery sheets:

$$V^s = V_1^s + V_2^s = V_{int} - V_{alk}. \qquad [2]$$

A combination of Eqs. [1] and [2] permits calculation of the size and composition of the nanophase reactor:

$$V_1^s = (V_{int} - V_{alk})\Phi_1 + (V_{m,1}\Phi_2 + V_{m,2}\Phi_1)n_1^{\sigma(n)}. \qquad [3]$$

The interlamellar volume per unit cell (nm^3/uc) is readily calculated from X-ray diffraction data:

$$V_{int} = A_{cell}(d_L - \delta). \qquad [4]$$

Here $A_{cell} = 0.232$ nm^2 is the crystal geometric surface area of an $[Si, Al]_4O_{10}$ unit and $\delta = 0.96$ nm is the thickness of the montmorillonite sheet (18). The volume of the alkyl chains per unit cell is $V_{alk} = 0.152$ nm^3/uc, which is equal to the molecular volume of the organic cation ($V_{HDA} = 0.474$ nm^3/molecule) multiplied by the surface charge density per unit cell of the clay ($\zeta = 0.32$/uc, as derived from the cation-exchange capacity of the montmorillonite) (18). Experimentally, the first term on the right-hand side of Eq. [3] is related to X-ray diffraction data, while the second term is obtained from liquid sorption measurements (Fig. 1). If the dimensions of the variables in Eq. [3] are carefully selected, the volume distribution of the various species (hexadecyl chains, toluene, and ethanol) in the clay galleries can be calculated, either per unit mass of organoclay or per $[Si,Al]_4O_{10}$ formula unit, as shown in Fig. 2.

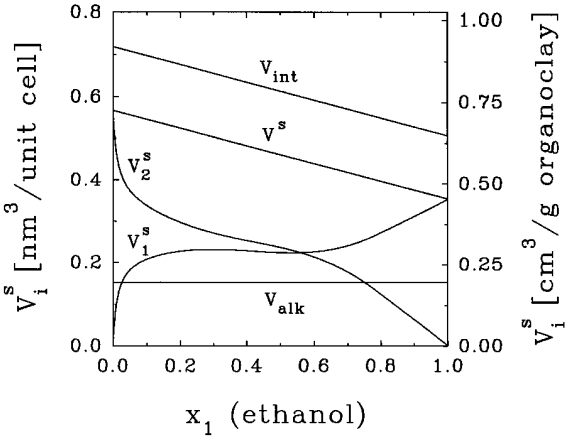

FIG. 2. Volume distribution in HDAM clay galleries as a function of the bulk liquid composition in ethanol–toluene mixtures. V_{alk}, alkyl chains; V_1^s, ethanol; V_2^s, toluene; V_{int}, interlamellar space; V^s , nanophase reactor.

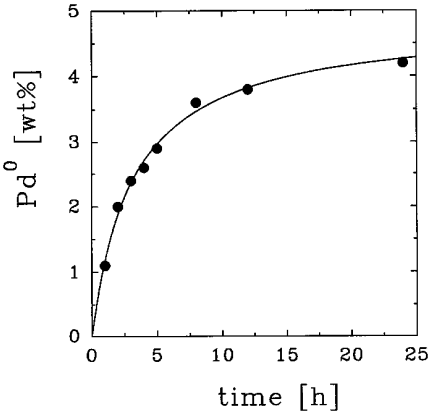

FIG. 4. Progress of Pd^0 formation in HDAM at 298 K in a reaction system of ethanol : toluene = 5 : 125 (v/v); $Pd(OAc)_2 = 0.23\%$; HDAM = 0.77%.

The volume of the nanophase reactor in equilibrium with a toluene-rich bulk liquid phase, which is of particular interest, is around 0.7 cm^3/g organoclay with an ethanol content of about 0.25 cm^3/g. Note that 10 mass% Pd^0 intercalated in HDAM would occupy a volume of less than 0.01 cm^3/g organoclay. The equilibrium composition of the nanophase reactor is plotted against the composition of the dispersion medium in Fig. 3. It can be seen that an ethanol mole fraction of $x_1 = 0.07$ in the bulk liquid phase is in equilibrium with an ethanol mole fraction of about $x_1^s = 0.5$ in the interlamellar space, corresponding to a separation factor of $S = x_1^s x_2 / x_1 x_2^s > 10$. This difference in ethanol concentration, i.e., the selective interlamellar sorption of ethanol, seems to be sufficient for the rate of Pd^{2+} reduction to be considerably higher in the nanophase reactor than in the bulk solution. On the other hand, x_1^s may be regarded as an average value, rather than a uniform value, throughout the interlamellar space. In fact, it is reasonable to assume that

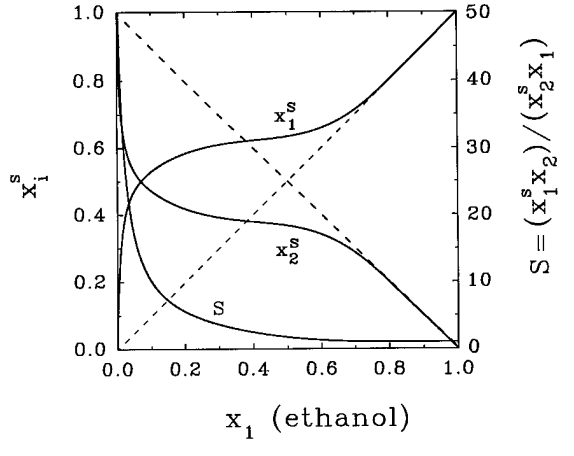

FIG. 3. Nanophase reactor–bulk liquid equilibrium phase diagram. S = separation factor; dashed lines: $x_i^s = x_i$.

the adsorption of the components is more or less localized, so that the hydrophobic alkyl chains are solvated by toluene molecules, while the ethanol molecules are predominantly accumulated in the close proximity of the hydrophilic silicate layers. A two-phase equilibrium has been claimed to exist for the adsorption of long-chain alcohols from *n*-heptane on a graphite surface (24), and a demixing tendency of alcohol–hydrocarbon liquid pairs in the adsorption layer of swelling and nonswelling organoclays has also been suggested (19–21). A demixing process of this kind (i.e., pure ethanol rather than an ethanol-rich environment) would act further in favor of Pd^0 formation followed by a possible particle deposition on the silicate surface. On addition of $Pd(OAc)_2$ to the clay suspended in ethanolic toluene solution, Pd^{2+} ions will diffuse from the bulk solution into the nanophase reactor and the reduction will proceed. Generation of Pd particles in the nanophase reactor as a function of reaction time is plotted in Fig. 4 for a given composition of the reactants. The $Pd(OAc)_2$ consumption was monitored spectrophotometrically as described under Synthesis. Four Pd^0–HDAM samples (2.5, 4.2, 6.5, and 10.4% Pd by mass) were selected for use and subjected to instrumental analysis in the same way as the original HDAM samples (Table 1).

Electron Microscopy

Evidence of the formation of Pd nanoparticles is demonstrated by the transmission electron micrographs (Fig. 5). The Pd particles are reasonably monodispersed with some crystalline appearance. It was generally observed that the particle size increased with increasing Pd content. A longer reaction time favored the formation of larger, more crystalline, and more polydispersed particles, which is attributable to simultaneous nucleation and growth processes. The average diameters of the Pd particles are listed in Table 1. Figures 5a and b show particles of average diameters 3.5 and 12.8 nm, respectively. An entire clay lamella is displayed in Fig. 5c.

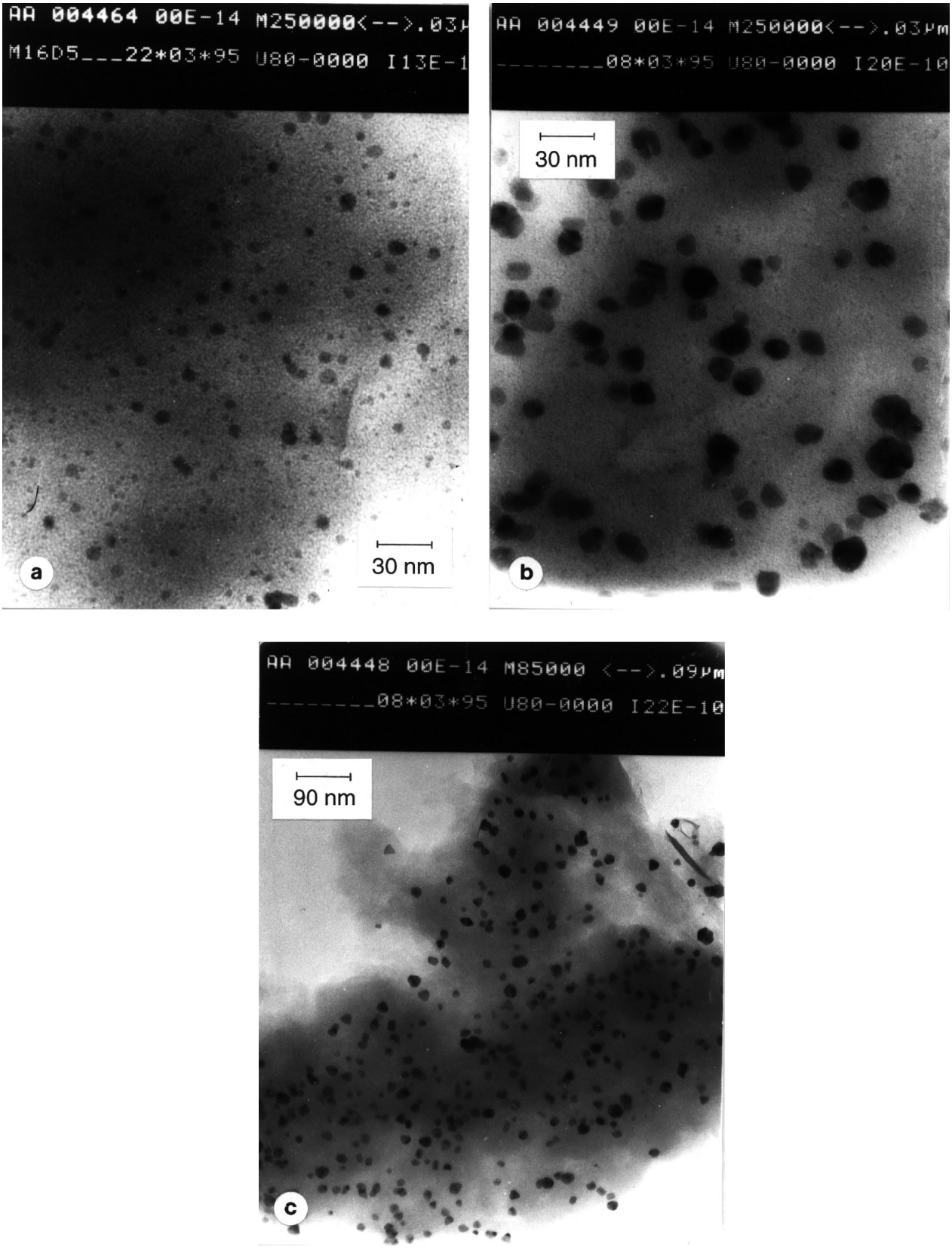

FIG. 5. Transmission electron micrographs of (a) 2.5% Pd^0–HDAM (×250,000); (b) 10.4% Pd^0–HDAM (×250,000); and (c) an isolated clay lamella, 10.4% Pd^0–HDAM (×85,000).

TABLE 1

Characterization of Pd^0–HDAM Clays by TEM, BET Surface Area Analysis, XRD, SAXS, and Low-Shear Rheology[a]

Pd^0 (wt%)	d (TEM) (nm)	a_s (BET) ($m^2\ g^{-1}$)	I_{rel} (XRD) $2\theta = 4.99°$	I_{rel} (XRD) $2\theta = 40.2°$	K_p (SAXS) (cps nm^{-3})	l_r (SAXS) (nm)	τ_B (mPa)
—	—	4.71	1.00	—	—	—	13.2
2.5	3.5	12.77	0.56	0.17	4.8	6.59	19.3
4.2	6.3	13.18	0.48	0.35	19.6	7.09	23.0
6.5	10.4	14.47	0.38	0.56	24.0	7.25	27.2
10.4	12.8	14.42	0.36	1.00	31.9	7.30	37.5

[a] Pd^0 (wt%): mass percent Pd in Pd^0–HDAM, obtained by means of VIS spectrophotometry; d (TEM): diameter of Pd particles, determined from transmission electron micrographs; a_s (BET): BET-specific surface area (standard deviations, $< 2.0\%$); I_{rel} (XRD), $2\theta = 4.99^0$: relative XRD peak intensity characteristic of HDAM [(001) reflection]; I_{rel} (XRD), $2\theta = 40.2^0$: relative XRD peak intensity characteristic of (111) Pd; K_P: Porod constant obtained from SAXS measurements; l_r: intersection length obtained from SAXS measurements; τ_B: Bingham yield stress of Pd^0–HDAM, 2% (w/v) in toluene, obtained by means of low-shear rheology.

BET Surface Area Analysis

The BET surface areas of Pd^0–HDAM samples are about three times that of HDAM (Table 1). The low specific surface areas of about 14 $m^2\ g^{-1}$ suggest that the structure of Pd^0–HDAM is quite different from the structure of pillared clays: for dry organoclay samples the internal surface sites are not accessible to the nitrogen molecules.

The crystal geometric (internal plus external) surface area of montmorillonite ($\sim$760 $m^2\ g^{-1}$) is about two orders of magnitude higher than the external surface area. The mosaic structure of the external surface of hexadecylpyridinium illite (HDPI) is remarkably similar to the mosaic structure of the surface of hexadecylpyridinium montmorillonite (HDPM) (21). Their BET surface areas are also close to each other. A major difference is that HDPI is a nonswelling mineral in contrast with HDPM. It follows that, unlike HDPM or HDAM in organic media, no internal surface sites are available for HDPI, and thus the size of the adsorption layer (nanophase reactor) provided by the ethanol(1)–toluene(2)/HDPI interface is expected to be considerably smaller. Accordingly, we performed a test reaction and experienced that, as HDAM was replaced with HDPI, under otherwise the same experimental conditions, the rate of Pd^{2+} consumption drastically diminished. This test reaction confirmed that for HDAM, both the internal and external surface sites must be involved in Pd particle generation and deposition.

XRD Measurements

X-ray diffraction (XRD) measurements on dry HDAM gave a (001) reflection at $2\theta = 4.99°$. This angle corresponds to $d_L = 1.77$ nm, which is slightly less than twice the alkyl chain cross section plus the thickness of the silicate layer. The peak position did not alter significantly for the Pd^0–HDAM samples, but the half-height peak-width slightly broadened while the intensity decreased with increasing Pd content (Table 1). Poorly crystalline, low-dispersity Pd particles obtained directly from ethanolic reduction of $Pd(OAc)_2$ gave a Bragg reflection at $2\theta = 40.2°$, characteristic of (111) Pd (25). This peak was absent for HDAM, but appeared for Pd^0–HDAM; the intensity varied in parallel with the Pd content (Table 1).

SAXS Measurements

Small angle X-ray scattering data in a log(I)-versus-log(h) representation are shown in Fig. 6 with a $\Delta I \times h^3$-versus-h^3 insert. The peaks positioned at about $\log(h/nm^{-1}) = 0.55$ correspond to the first-order (001) Bragg reflection of HDAM. The Porod plots (insert in Fig. 6) permitted the reduced chord length (or intersection length) l_r to be calculated (26–28). If phase 1 is dispersed in phase 2, a line crossing through the system cuts out alternating chords l_1 and l_2 from the two regions. The mean lengths are distributed in the proportion of the two respective volume fractions: $l_1 : l_2 = \Phi_1 : \Phi_2$. The intersection length l_r is related to the lengths of the chords by $1/l_r = 1/l_1 + 1/l_2$, and thus in a dilute system ($\Phi_1 \ll \Phi_2 \approx 1$), l_r becomes equal to

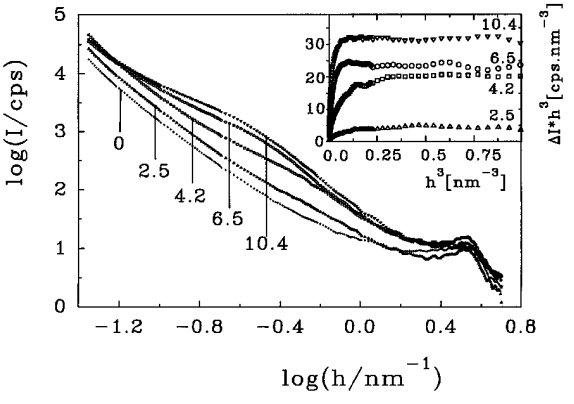

FIG. 6. Log–log representation of normalized SAXS intensities as a function of the scattering wavevector. Insert: Porod plots. The Pd^0 contents of the Pd^0–HDAM samples are indicated in the figure in mass percent.

l_1. In general, the intersection length of the ith phase can be calculated as (26, 27)

$$l_i = \frac{M_1}{(1-\Phi_i)K_P} = \frac{\int_0^\infty \Delta I(h)h\,dh}{(1-\Phi_i)\lim_{h\to\infty}\Delta I(h)h^3}, \qquad [5]$$

where M_1 is the first moment of the scattering intensity, and K_P is the constant of Porod (28). For the present systems $\Phi_{Pd} \ll \Phi_{HDAM}$ and l_r may be regarded as a measure of the size of the Pd particles in the HDAM matrix. It should be stressed that, in contrast with transmission electron microscopy, SAXS provides information on both the internal and external surface sites. The values obtained for K_p and l_r are collected in Table 1.

Low-Shear Rheology

The flow curves of low-shear rheological measurements on 2% clay suspensions in toluene are given in Fig. 7. The Bingham yield value τ_B, obtained from extrapolation of the τ-versus-D plot to zero shear rate (intercept), is proportional to the adhesion between the clay sheets. As is to be seen in Table 1, τ_B increases with increasing Pd concentration. This trend indicates stronger interparticle interactions due to Pd bridging the clay lamellae. As the structure of the lamellae is destroyed at higher shear rates ($D > 20$ s^{-1}), the plastic viscosity of the suspensions (slope of the straight lines) becomes apparently independent of Pd concentration ($\sim$0.76 mPa · s).

Structure and Catalytic Applications of Pd^0–HDAM

The formation of Pd nanoparticles between the hydrophobized montmorillonite layers modifies the orientation of the lamella packages. The apparently unaltered XRD peak positions, along with the broadening and the decrease in XRD intensities, suggest that a regular intercalation of Pd particles in the clay galleries is unlikely. Variation of the basal spacings ranging from 2 to 4 nm could be achieved by variation of the solvent composition, similarly as for HDAM. Since considerably less Pd^0 was generated on nonswelling HDPI organoclays, Pd particle formation for the swelling HDAM may be expected to occur in the gallery region as well as (or rather than) on the external surface sites. An increase in BET surface area with respect to the original HDAM sample indicated distortion of the closely packed, parallel arrangement of the clay lamellae. Furthermore, low-shear rheology indicated that the nanosized particles form bridges between the lamellae. Inspection of the pure supernatant of the organoclay suspension revealed that Pd is not leached out even at high shearing rate. This is an important observation from the viewpoint of catalytic applications. Taking the above arguments into consideration, we propose a model in which most of the Pd particles occupy defect sites in the clay aggregates, as shown in Fig. 8. Similar structure was suggested by Giannelis *et al.* for ruthenium particles intercalated in alumina-pillared montmorillonite (29). These defect sites may be formed by layer folding and the formation of interfaces between discrete clay layers.

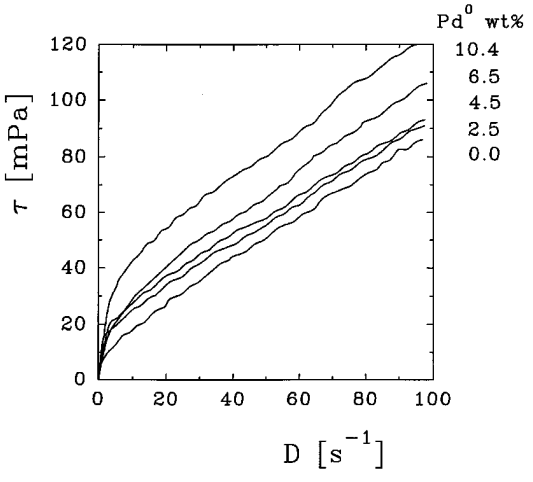

FIG. 7. Shear stress plotted against shear rate gradient for 2% Pd^0–HDAM suspensions in toluene. The Pd^0 contents of the organoclay samples are indicated on the graph in mass percent.

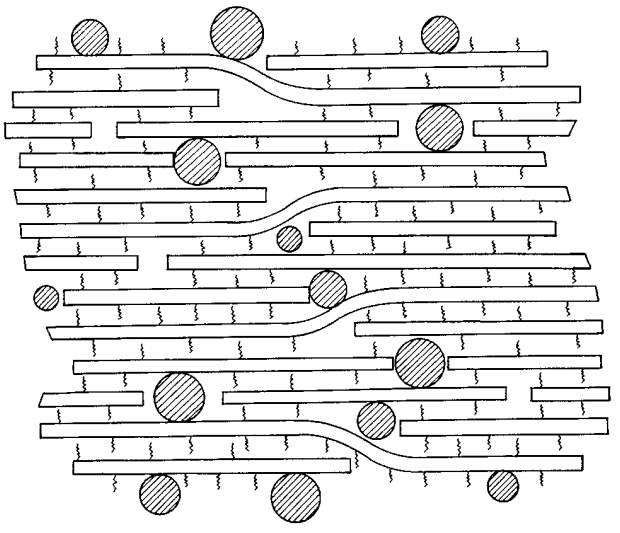

FIG. 8. Schematic illustration of the proposed arrangement of palladium nanoparticles between swollen HDAM clay layers suspended in a good solvent. Tails represent hexadecyl chains.

The Pd^0–HDAM samples in suspension proved to be catalytically active in the hydrogenation of alkenes. The rates of 1-octene and styrene hydrogenation in various solvents were determined with a conventional hydrogenation apparatus at atmospheric pressure at 298 K. A supported catalyst, 3% Pd on Cab-O-Sil (Pd–CBS), was also used for comparison. Typically, the reaction vessel contained 1 cm^3 of solvent, 5 mg of catalyst, and 0.05 to 0.2 cm^3 of substrate. The applied stirring rate (1240 rpm) was found to

be fast enough to eliminate diffusion control. The reaction was conducted until completion and the products were then identified by GLC. In the knowledge of the average particle size and on the assumption that 1 m^2 of Pd comprises 1.2×10^{19} atoms (30), the number of exposed Pd atoms can be calculated for various particle geometries. Turnover frequencies (TOFs) were computed from the initial hydrogen uptakes (5–10 min). Assuming cubic geometry with five exposed faces, the hydrogenation of 1-octene in toluene afforded TOF values of 1.97 and 0.50 s^{-1} for 4.2% Pd^0–HDAM and 3% Pd–CBS, respectively. Hydrogenation of styrene to ethylbenzene in ethanol yielded 2.32 s^{-1} for 2.5% Pd^0–HDAM and 2.54 s^{-1} for 3% Pd–CBS. These preliminary results confirm that the Pd^0–HDAM samples are efficient hydrogenation catalysts. A systematic study on the catalytic reactivity of Pd–organoclays is currently being undertaken.

It is to be noted that Pd^0–HDAM is suitable for contact catalytic hydrogenation reactions in the liquid phase, which swells the clay and opens access to the Pd. However, the synthetic route described under Experimental has been successfully applied to classic solid matrixes so that *in situ* preparation technique offers an alternative to the conventional impregnation methods. For example, we generated Pd particles on sodium montmorillonite and alumina-pillared montmorillonites (0.5–2.5 wt% in a reaction time of less than 4 h). For these materials, catalytic implications in gas-phase reactions are anticipated.

CONCLUSIONS

This paper has described a rational design of nanophase reactors at the solid/liquid interface, suitable for the *in situ* preparation of palladium nanoparticles incorporated into smectite clays. The selective sorption of ethanol from toluene in the interlamellar space of organophilized montmorillonite, where ethanol functions as a reducing agent for palladium (II) acetate, ensures the nucleation and growth of metallic palladium particles, with subsequent deposition on the silicate surface of the clay. The Pd–organoclay is catalytically active in the liquid phase hydrogenation of alkenes. This novel preparation method can readily be extended to other catalyst supports and to other noble or transition metals, including alloys. The basic principles of the controlled colloid synthesis described here can be applied in other fields of material science.

ACKNOWLEDGMENT

Partial support of this research by the Hungarian Scientific Research Foundation through Grant OTKA T007530 is gratefully acknowledged.

REFERENCES

1. Balogh, M., and Laszlo, P., "Organic Chemistry Using Clays." Springer-Verlag, Berlin/Heidelberg, 1993.
2. Pinnavaia, T. J., *Science* **220**, 365 (1983).
3. Occelli, M. L., *in* "Proceedings of the International Clay Conference" (L. G. Schultz, H. van Olphen, and F. A. Mumpton, Eds.), p. 319. Clay Mineral Society, Bloomington, IN, 1987.
4. Yamanaka, S., Nishihara, T., Hattori, M., and Suzuki, Y., *Mater. Chem. Phys.* **17**, 87 (1987).
5. Choudary, B. M., and Rani, S. S., *J. Mol. Catal.* **75**, L7 1992.
6. Guiu, G., and Grange, P., *J. Chem. Soc. Chem. Commun.*, 1729 (1994).
7. Pinnavaia, T. J., Tzou, M.-S., Landau, S. D., *J. Am. Chem. Soc.* **107**, 4783 (1985).
8. Pinnavaia, T. J., *in* "Preparative Chemistry Using Supported Reagents" (P. Laszlo, Ed.), Chap. 25, p. 483. Academic Press, San Diego/London, 1987.
9. Johnson, I. D., Werpy, T. A., and Pinnavaia, T. J., *J. Am. Chem. Soc.* **110**, 8545 (1988).
10. (a) Parulekar, V. N., and Hightower, J. W., *Appl. Catal.* **35**, 249 (1987); (b) *Appl. Catal.* **35**, 263 (1987).
11. Ravikumar, K., Choudary, B. M., Jamil, Z., and Thyagarajan, G., *J. Chem. Soc. Chem. Commun.*, 130 (1986).
12. Choudary, B. M., and Bharathi, P., *J. Chem. Soc. Chem. Commun.,* 1505 (1987).
13. Khan, M. M. T., Samad, S. A., and Siddiqui, M. R. H., *J. Mol. Catal.* **50**, 97 (1989).
14. Mazzei, M., Marconi, W., and Riocci, M., *J. Mol. Catal.* **9**, 381 (1980).
15. Raythatha, R., and Pinnavaia, T. J., *J. Organomet. Chem.* **218**, 115 (1981).
16. Boonekamp, E. P., Kelly, J. J., and Fokkink, L. G. J., *Langmuir* **10**, 4089 (1994).
17. Esumi, K., Itakura, T., and Torigoe, K., *Colloids Surf.* **82**, 111 (1994).
18. Dékány, I., Turi, L., Tombácz, E., and Fendler, J., *Langmuir* **11**, 2285 (1995).
19. Dékány, I., Szántó, F., Weiss, A., and Lagaly, G., *Ber. Bunsenges. Phys. Chem.* **89**, 62 (1985).
20. (a) Dékány, I., Szántó, F., Weiss, A., and Lagaly, G., *Ber. Bunsenges. Phys. Chem.* **90**, 422 (1986); (b) *Ber. Bunsenges. Phys. Chem.* **90**, 428 (1986).
21. (a) Dékány, I., Szántó, F., and Nagy, L. G., *J. Colloid Interface Sci.* **103**, 321 (1985); (b) *J. Colloid Interface Sci.* **109**, 376 (1986).
22. Everett, D. H., *Pure Appl. Chem.* **58**, 967 (1986).
23. Kipling, J. J., "Adsorption from Solution of Non-Electrolytes." Academic Press, London/New York, 1969.
24. (a) Findenegg, G. H., Koch, C., and Liphard, M., *in* "Adsorption from Solution" (R. H. Ottewill, C. H. Rochester, and A. L. Smith, Eds.), p. 87. Academic Press, London/New York, 1983; (b) Bien-Vogelsang, U., and Findenegg, G. H., *Colloids Surf.* **21**, 469 (1986).
25. Carturan, G., Facchin, G., Cocco, G., Enzo, S., and Navazzo, G., *J. Catal.* **76**, 405 (1982).
26. Kratky, O., and Laggner, P., *in* "Encyclopedia of Physical Science and Technology" (R. A. Meyers, Ed.), Vol. 14, p. 693. Academic Press, London/New York, 1987.
27. "Small Angle X-ray Scattering" (O. Glatter and O. Kratky, Eds.). Academic Press, London/New York, 1982. (Overview on the entire field of X-ray small-angle scattering, presented in 15 chapters, on 515 pages, by 13 authors.)
28. (a) Porod, G., *Kolloid-Z.* **124**, 83 (1951); (b) *Kolloid-Z.* **125**, 51 (1952).
29. Giannelis, E. P., Rightor, E. G., and Pinnavaia, T. J., *J. Am. Chem. Soc.* **110**, 3880 (1988).
30. Aben, P. C., *J. Catal.* **10**, 224 (1968).